doi:10.26443/seismica.v3i2.1205

SEISMICA

Earthquake Moment Magnitudes from Peak Ground Displacements and Synthetic Green's Functions

Torsten Dahm * [1,2], **Daniela Kühn** [1,3], **Simone Cesca** [1,2], **Marius Isken** [1], **Sebastian Heimann** [2]

[1]Physics of Earthquakes and Volcanoes, GFZ German Research Centre for Geosciences, Potsdam, Germany, [2]Institute for Earth and Environment, University of Potsdam, Potsdam, Germany, [3]Applied Seismology, NORSAR, Kjeller, Norway

Author contributions: *Conceptualization*: Torsten Dahm. *Methodology*: Torsten Dahm, Sebastian Heimann. *Software*: Sebastian Heimann, Marius Isken. *Validation*: Torsten Dahm, Daniela Kühn, Simone Cesca. *Writing - Original draft*: Torsten Dahm. *Writing - Review & Editing*: Daniela Kühn. *Visualization*: Torsten Dahm, Daniela Kühn, Simone Cesca, Marius Isken.

Abstract We suggest an approach employing full waveforms from synthetic seismograms to estimate moment magnitudes and their uncertainties from peak amplitudes. The new method is theoretically derived. It does not change the established routines of traditional procedures for magnitude determination, while overcoming some limitations such as saturation, scattering and source complexity. Attenuation functions and their uncertainties are derived from synthetic seismograms using Green's function databases representing various velocity models if required. In a bootstrap approach, source geometry and dynamic and kinematic parameters are randomly selected within a realistic range. After calibration with observations, attenuation functions can be extrapolated to distances, depths, regions and magnitudes for which no observations exist. Additionally, individual frequency filters and sensor types can be mixed independently of any definition of traditional magnitude scales including the sensor characteristics and its potential frequency saturation. Uncertainties of attenuation functions are estimated for every source-station geometry. For this, bootstrap results are averaged over a configurable range of distance and depth. Therefore, realistic uncertainties of mean magnitudes can be estimated even in case of only few measurements. The method is especially useful for estimating local and moment magnitudes for temporary deployments or monitoring induced seismicity in regions with only a few tectonic events.

Resumen Se propone un método para estimar la magnitud momento y su incertidumbre basado en la amplitud máxima de sismogramas sintéticos. El procedimiento se ha desarrolado a partir de la formulación teorica. El método propuesto sigue el enfoque tradicional, pero soluciona algunas de sus limitaciones, tal como la saturación, scattering y complejidad de la fuente sísmica. Las funciones de atenuación y sus incertidumbres se derivan de sismogramas sintéticos calculados mediante bases de datos de funciones de Green, pudiendo considerar diferentes modelos de velocidad. Siguiendo un enfoque bootstrap, parámetros como la profundidad, parámetros cinemáticos y dinámicos, caída de esfuerzos y velocidad de ruptura se seleccionan de forma aleatoria dentro de intervalos realistas. Después de su calibración con algunas observaciones, las funciones de atenuación pueden extrapolarse a otras distancias, profundidades, magnitudes y regiones. Pueden combinarse fltros en frecuencias y diferentes tipos de sensores, independientemente de las definiciones de las mangitudes tradicionales, teniendo en cuenta las características de los sensores y sus frecuencias de saturación. Las incertidumbres de las funciones de atenuación se estiman para cada fuente-estación. A este fín, se realiza un promedio de los resultados del bootstrap, para un conjunto configurable de distancias epicentrales y profundidades focales. Esto permite estimaciones realistas de las incertidumbres aún con pocas observaciones. El método es especialmente útil para estimar magnitud local y magnitud momento durante instalaciones temporales, y por el monitoreo de la sismicidad inducida en regiones con poca sismicidad tectónica.

摘要 我们提出了一种方法，利用合成地震图的全波形，从峰值振幅估算矩震级及其不确定性。新方法不改变传统震级确定程序的既定流程，同时克服了饱和、散射和震源复杂性等局限性。如果需要，可使用针对各种速度模型得出的格林函数数据库，从合成地震图中为每个震源台站组合即时推导衰减函数及其不确定性 。震源深度、几何形状、及动态和运动学参数利用 bootstrap 方法在合理范围内随机选择。根据观测数据进行校准后，衰减函数可外推到没有观测数据的距离、深度、区域和震级。此外，各个频率滤波器和地震仪类型可以混合使用，而不受传统震级尺度定义甚至仪器特性及其可能的频率饱和的影响。衰减函数的不确定性是根据每个震源台站的几何位置估算的，正因如此，bootstrap 的结果取为可设置的距离和深度范围的平均值, 从而即使只有很少的测量数据，也能估算出平均震级的实际不确定性。该方法尤其适用于利用流动台站估算近震震级和矩震级，或用于监测仅有少量构造事件的地区的诱发地震。

Production Editor:
Gareth Funning
Handling Editor:
Andrea Llenos
Copy & Layout Editor:
Hannah F. Mark

Signed reviewer(s):
Andreas Steinberg

Translated by:
Xueqing Li
Simone Cesca

Received:
February 2, 2024
Accepted:
November 25, 2024
Published:
December 19, 2024

*Corresponding author: dahm@gfz-potsdam.de

Non-technical summary One way to measure the size of an earthquake is its moment magnitude, a quantity related to the seismic moment which accurately describes the size of and displacement along the fault on which the earthquake occurred. Since it is often difficult to derive moment magnitudes for earthquakes with low magnitudes and therefore noisy records, the local magnitude scale was introduced almost 100 years ago as an empirical scale relying on peak amplitudes of seismic waves. However, it suffers from several limitations related to complexity of fault geometry, the medium the earthquake waves propagate through, and the instruments recording the waves. Especially if only few events are observed, the attenuation of amplitudes from source to receiver is challenging to estimate. We overcome this problem by extending the data set of observations with synthetic seismograms, expanding the calculations to source-station distances, earthquake depths, source regions and magnitudes for which no observations exist, while allowing the use of the more precise moment magnitude also for local earthquakes. In addition, the uncertainties of magnitudes can be estimated reliably even in case of only few existing measurements. This will allow better characterization of seismicity caused by human activities in the subsurface, which often takes place in areas with little natural earthquake activity at unusual shallow depths.

1 Introduction

Magnitudes are a concept to measure the relative strength of earthquakes under a point source assumption. They are traditionally derived from peak amplitudes of seismograms normalised by the expected peak amplitude of a reference source. The first magnitude scale, the local magnitude $\mathrm{M_L}$, was introduced by Richter (1935) for Southern California. It was defined as the logarithm of the peak ground displacement (PGD) of a seismogram recorded by a Wood Anderson instrument normalised by the expected peak displacement of a reference event with magnitude $\mathrm{M_L}$=0. This magnitude scale requires a knowledge of the empirically derived normalisation function of the reference event, the so-called distance attenuation function a_0 of peak amplitudes. a_0 depends on the local crustal structure and should be estimated for every region individually from a number of earthquake recordings. However, in practice, the original attenuation function by Richter (1935) is often adopted. For instance, Browitt (1999) compiled attenuation relations and magnitude procedures from more than 24 data centres in Europe and Asia resulting in more than 30 individual implementations and attenuation relations, often with only scant documentation. Between 1935 and 2012, more than 14 additional magnitude scales have been introduced, almost all following a similar concept and defining their own attenuation functions, in which PGD is measured on specific real or simulated instruments either on bandpass-filtered displacement or velocity seismograms.

Newer methodological developments aim to better calibrate local magnitude scales. For example, Al-Ismail et al. (2023) correct peak amplitudes to a reference distance of 10 km deriving attenuation curves from synthetic seismograms for narrow frequency bands. Luckett et al. (2018) correct a discrepancy between local magnitudes calculated at stations less than 10 km away compared to more distant stations by including a new exponential term in the general form of the local magnitude scale. Other scales than $\mathrm{M_L}$ often divide peak amplitudes by the associated dominant period of the wave. The different scales cover a broad range of epicentral distances, earthquake strengths and wave frequencies. An extensive review of magnitude scales is given in the New Manual of Seismological Observatory practice (NMSOP2, Bormann et al., 2013) and in Utsu (2002).

The strength of the magnitude approach is that peak amplitudes can be easily and robustly measured, even in case of moderate and poor signal-to-noise ratios. On the other hand, magnitude scales suffer from many weaknesses, e.g. the saturation problem, limitations depending on sensor and instrument response, the oversimplification of attenuation functions excluding source rupture, radiation or station site effects, uncertainty estimates in the case of only few observations, and the non-compatibility of magnitudes derived by different observatories. Thus, although magnitude determination and earthquake location are the most basic parameters routinely communicated by observatories, the understanding of the diverse magnitude scales and their differences is confusing not only to the public, but also for scientists outside the community.

In contrast, the seismic moment $\mathrm{M_0}$ (Aki, 1966) is an independent measure of earthquake strength based on physical parameters of the source. $\mathrm{M_0}$ is measured from the low frequency plateau of the source spectra. The seismic moment overcomes many of the limitations of the empirical magnitude scales. From the logarithm of $\mathrm{M_0}$, a dimensionless moment magnitude $\mathrm{M_w}$ was defined (Kanamori, 1977; Purcaru and Berckhemer, 1978; Hanks and Kanamori, 1979), which theoretically scales linearly with $\mathrm{M_S}$ and many other magnitude scales, and therefore provides a parameter suitable for communication to the public. However, since $\mathrm{M_0}$ is more difficult to estimate during routine processing, especially for weak earthquakes, $\mathrm{M_L}$ is still the standard measure of strength for small magnitude events. However, Stork et al. (2014) note that even estimates of $\mathrm{M_w}$ may vary substantially depending on the method and parameters employed for their calculation. Further, they point out that errors in magnitudes are rarely reported, although both their existence and size is of considerable importance especially for magnitude-dependent traffic light systems introduced to detect unstable processes early in the evolution of induced seismicity.

Seismic hazard, risk and ground shaking studies nowadays rely more and more on $\mathrm{M_w}$ due to its global comparability independent of empirical attenuation functions. Therefore, relations between $\mathrm{M_w}$ and $\mathrm{M_L}$ (or other magnitude scales) have been derived for several regions and seismological catalogues, in order to provide an unbiased database. Based on theoretical rupture models, Deichmann (2006) showed that the expected scaling between $\mathrm{M_L}$ and $\mathrm{M_w}$ is linear with a slope of 1. Fig. 1 shows a compilation of observed $\mathrm{M_L}$-$\mathrm{M_w}$ scaling relations. The scaling is often non-linear and the differences between individual scales can be larger than 0.5 magnitude units. Boore (1989) showed that a systematic difference of up to 0.4 magnitude units is obtained for short distances of 0-30 km, if attenuation curves are extrapolated and site-specific attenuation is not considered. Disregarding damping and scattering may lead to a distance-dependent bias in a_0, which may affect both larger and smaller magnitude events. For example, multiple reflected SH waves that build up to Lg Love waves can dominate the horizontal ground motion amplitudes at regional distances for frequencies >0.5 Hz and may not be included in the attenuation models. Butcher et al. (2020) demonstrate that the $\mathrm{M_L}$-$\mathrm{M_w}$ relationship at New Ollerton can only be correctly captured by incorporating high-frequency attenuation into the source model, reducing the influence of stress drop on the gradient. Apart from attenuation and scattering, differences in scaling can be related to variations in source properties, such as stress drop and rupture velocity (see e.g., Deichmann, 2006, 2017). For small magnitude earthquakes in regions where only few local records are available, radiation pattern and directivity effects will not average out and may lead to biases and variation in $\mathrm{M_L}$ (e.g. Daniel, 2014), easily adding up to one magnitude unit.

Waveform modelling and the analysis of synthetic seismograms can help to reduce the bias as well as large variations in magnitudes. Duda and Yanovskaya (1993) as well as Jansky et al. (1997) suggested using synthetic seismograms to estimate spectral amplitudes, to improve earthquake strength estimation. However, the proposed modelling was relatively simple and the approach was not adapted for routine processing. During the last decades, the methods to determine and employ synthetic seismograms have improved enormously and are now able to produce realistic full waveform seismograms, even when employing personal computers. For instance, if Green's functions (GF) are calculated in advance (e.g. Heimann et al., 2019), hundreds and thousands of seismograms can be computed within a few minutes varying source and station parameters. Al-Ismail et al. (2020) employed synthetic Wood Anderson seismograms, taking into account source mechanism, corner frequencies, and the ω^2 source spectrum, to estimate an attenuation curve for southern Kansas and calibrate $\mathrm{M_L}$ to $\mathrm{M_w}$.

In the following, we will demonstrate the application of such an approach and suggest probing both source and model parameter spaces to estimate expected peak amplitudes and their uncertainties at each station. Depending on the available information, the sampling range can be constrained and thus, uncertainties reduced. Further, the approach can easily be implemented in existing analysis codes and help to estimate unbiased magnitudes for temporary deployments and regions for which only few seismological recordings exist. In addition, it offers the possibility to include stations and sensors that are not considered in traditional methods for magnitude computation, such as borehole chains, fibre optic cables, ocean bottom seismometers, or hydrophones. It may also serve to analyse unusual earthquakes sources, for instance at very shallow or very large depths, that are not well captured by traditional magnitude scales. Because of the comparability of magnitudes and their uncertainties, we especially recommend using this methodology for implementation of traffic light systems in industrial operations.

The paper is structured as follows: in Section 2, we provide the theoretical background and justification of the peak amplitude approach for $\mathrm{M_w}$. Details of the modelling concept and the employed toolbox are described in Section 3. Subsequently, we provide two applications in Section 4 and discuss the results.

2 Theoretical background

The dimensionless moment magnitude $\mathrm{M_w}$ is defined by two thirds of the logarithm of the seismic moment $\mathrm{M_0}$ normalised by the moment of a reference event $\mathrm{M_0^{(ref)}}$ (Kanamori, 1977; Hanks and Kanamori, 1979):

$$M_w \;=\; \log_{10}\left[\frac{M_0}{M_0^{\mathrm{ref}}}\right]^{2/3} = \frac{2}{3}\log_{10}\left[\frac{M_0}{M_0^{\mathrm{ref}}}\right] \qquad (1)$$

with M_0^{ref}=1.12·10^9 Nm. The seismic moment itself is a physical measure of earthquake strength and defined by Aki (1966) as

$$M_0 \;=\; \mathcal{N}\,\langle\Delta u\rangle\, A \;=\; \frac{16}{7}\Delta\sigma a^3\,, \qquad (2)$$

where $\langle\Delta u\rangle$ is the average displacement over the fault, A is the rupture area and $\mathcal{N}$ the rigidity of the rock mass at the source. The second equivalence is valid for a self-similar, circular rupture model (Sato and Hirasawa, 1973; Udías et al., 2014), where $\Delta\sigma$ is the stress drop and a the radius of the circular rupture plane. Seismic moments are usually estimated from the low frequency plateau of the amplitude spectra of body wave pulses after correction for theoretical propagation effects (e.g., Udías et al., 2014) or by fitting low-pass filtered waveforms to theoretical seismograms. However, here we use a different approach and estimate $\mathrm{M_w}$ from peak amplitudes, which is not as accurate as the aforementioned methods, but instead can be linked to established procedures for magnitude estimation.

The ground displacement $\mathbf{u}$ of a body wave train recorded at a station far from the source can be approximated by (e.g., Aki and Richards, 2002)

$$u_i(\mathbf{x},t) \;\approx\; \dot{M}_0(t) * \left[\hat{M}_{jk} G_i^{j(ff)}(\mathbf{x},\boldsymbol{\xi_0},t) s_k\right] \qquad (3)$$

with

$$\dot{M}_0(t) \;=\; \mathcal{N}\langle\Delta\dot{u}\rangle \int_A S(t-\frac{r_0-(\boldsymbol{\xi}\boldsymbol{\gamma})}{v})\, dA\,, \qquad (4)$$

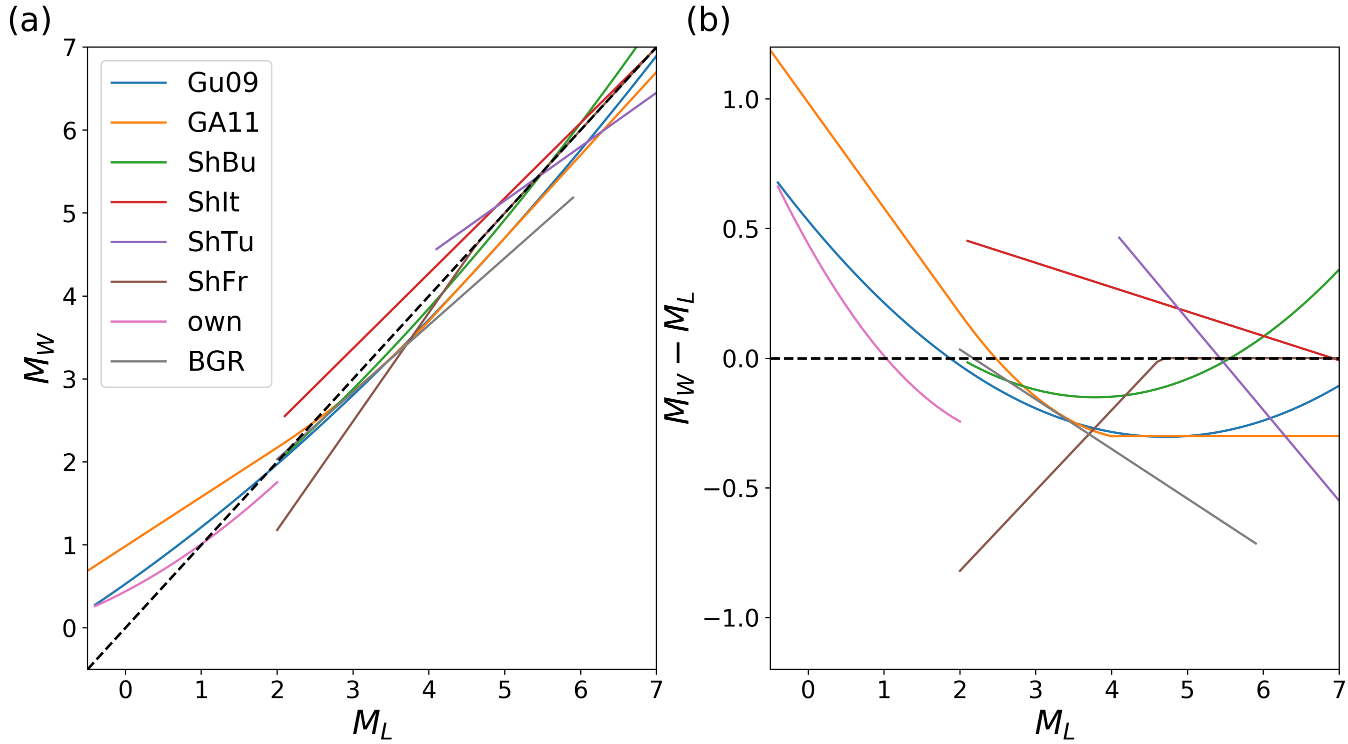

Figure 1 Examples of empirical $\mathrm{M_L}$-$\mathrm{M_w}$ scaling relations (a) and their residuals (b) for different regions in Northern Europe: Gu09=Grünthal et al. (2009); GA11=Goertz-Allmann et al. (2011); ShBu, ShIt, ShTu and ShFr established by SHARE project for Bulgaria, Italy, Turkey and France, respectively (see e.g., Grünthal et al., 2013); BGR developed for Germany (D. Kaiser, pers. comm.); *own* developed for mining area HAMM in this study.

where the asterisk indicates a temporal convolution integral. r_0 is the distance from the source centroid to the receiver with position vectors $\boldsymbol{\xi}_0$ and $\mathbf{x}$, respectively; $\boldsymbol{\xi}$ denotes the position at any point on the extended fault. $\langle\Delta\dot{u}\rangle$ is the average slip rate over a fault with area $A = \int d\xi_1 d\xi_2$. The ray direction is denoted by unit vector $\boldsymbol{\gamma}$. The moment rate function $\dot{M}_0(t)$ has been introduced as a point source representation of the average temporal evolution of the rupture, as seen in the far field. $S(t)$ is the normalised slip rate function. $\mathbf{G}^{(ff)} \cdot \mathbf{s}$ is the far field Green's tensor (for notation, see Dahm and Krüger, 2012), which summarises all wave propagation effects between source and receiver. The radiation pattern of the source is represented by the normalised moment tensor $\hat{\mathbf{M}}$. The factor $[\ldots]$, to which the summation convention has to be applied over the Cartesian components defined by the indices i, j and k, combines radiation pattern and wave propagation and has the physical unit of s/N. The slip rate function of a self-similar crack (Sato and Hirasawa, 1973; Udías et al., 2014) can be used to integrate eq. (3) to obtain an analytical solution for the ground displacement (e.g., Udías et al., 2014). From this, the ground peak displacement of the body wave pulse is given by (e.g. Udías et al., 2014)

$$\hat{u}_i \;=\; u_i(t=t_1) \;\approx\; \frac{48}{7}\Delta\sigma a^2 v_r \cdot w \cdot \hat{g}_i\,, \quad (5)$$

at time

$$t_1 \;=\; \tau + \frac{a}{v_r}\left(1 - \frac{v_r}{c}\cos\vartheta\right) \text{ with}$$

$$\hat{g}_i \;=\; \left[\hat{M}_{jk} G_i^{j(ff)}(t=t_1) s_k\right] \text{ and}$$

$$w \;=\; \frac{1}{\left[1 + \frac{v_r}{c}\cos\vartheta\right]^2},$$

where τ is the traveltime of the wave from the centroid to the receiver, v_r is the rupture velocity, c is the speed of the body wave, and ϑ is the latitude (polar angle minus $90°$) of the ray measured with respect to the source plane. w is a dimensionless factor accounting for directivity effect on peak amplitudes. For a rupture velocity of $v_r \approx 0.7c$, it varies between 0.35 and 11. Due to the circular growth of the rupture front, there is no azimuthal dependence in the directivity. However, if the rupture plane were to dip, the apparent source duration would also change with station azimuth. The factor $\hat{g}_i$ is the peak displacement of the i-th component of the seismogram synthesised from GFs and normalised moment tensor components, in order to consider the radiation pattern of the source. The peak amplitudes can be estimated in different frequency bands after synthetic data have been filtered. Note also that the circular rupture model implicitly reproduces the ω^{-2} spectral decay of the source time function at high frequencies (e.g. Udías et al., 2014), which is predicted in the model of Brune (1970), if an apparent rise time of ≈ 1.5 times the rupture time is used (Fig. S1 in the supplementary material).

Eliminating the source radius a with the help of eq. (2) gives

$$\hat{u}_i \;= M_0^{2/3} \cdot 3\left(\frac{16}{7}\Delta\sigma\right)^{1/3} v_r \cdot w \cdot \hat{g}_i\,. \quad (6)$$

Eq. (6) is valid for each component i of the displacement. To simplify the notation we omit the component i in the following. Eq. (6) can in principle be used to estimate M_0 from peak amplitudes $\hat{u}$, if peak amplitudes $\hat{g}$ from appropriate synthetic seismograms are known, directivity effects w are considered, and stress drop $\Delta\sigma$ as well as rupture velocity v_r are known. However, the scatter of peak amplitudes is very large and the approach is not very stable, especially if peaks are measured at high frequencies. Additionally, the radiation pattern may lead to positive and negative peak amplitudes, and the application of eq. (6) becomes intricate if the radiation pattern is unknown. We therefore follow an average intensity approach similar to the one established for magnitude scales, which builds on a reference attenuation function of absolute values of peak amplitudes by averaging over many different "observations", and the normalisation of the measured intensity of the PGD to derive individual station-magnitudes. If a sufficient number of stations recorded the earthquake, the average from all station-magnitudes is defined as event magnitude. However, in contrast to traditional magnitude scales, we estimate attenuation functions and their specific uncertainties from randomised synthetic seismograms. In addition to the common practice in magnitude estimation we then fully exploit the intrinsic uncertainties in all source and structural parameters, which are consequently propagated to the magnitude uncertainties.

We assume that we have measured PGD, $\hat{u}$, at N stations at different distances and different azimuths. Similarly to magnitude scales, we use absolute values of PGD to ensure positive values for the argument of the logarithms. For every station (at distance r), we define an average reference PGD from synthetic seismograms $|\hat{u}_{\mathrm{syn}}|$ for a hypothetical source with a moment magnitude $M_0^{(\mathrm{r})}$ close to the one of the earthquake, and with randomised source parameters with respect to source depth, stress drop and rupture velocity. If K is the number of synthetic source realisations, we define the mean of the absolute value of the peak amplitude and the variance Var of its logarithm by

$$\begin{aligned} |\hat{u}_{\mathrm{syn}}|(r) &= |\hat{u}_{\mathrm{syn}}| = \\ & (M_0^{(\mathrm{r})})^{2/3} \cdot \left\langle 3\left(\frac{16}{7}\Delta\sigma\right)^{1/3} v_r \cdot w \cdot |\hat{g}| \right\rangle \\ & \text{and} \\ \mathrm{Var} &= \frac{1}{K-1}\sum_{k=1}^{K}\left(\log_{10}|\hat{u}^{(k)}| - \log_{10}|\hat{u}_{\mathrm{syn}}|\right)^2 , \end{aligned} \tag{7}$$

where $\langle \dots \rangle$ denotes the mean of the distribution of K synthetic data realisations. For numerical implementation, we calculate for every station distance many hundreds of seismograms, varying source depth and rupture velocity in a reasonable range around hypocentral depth and 0.9 times the shear wave velocity, modifying $\Delta\sigma$ between 1 and 10 MPa, and altering the double couple moment tensor orientation uniformly in all directions. Since absolute values of peak amplitudes are used, the distribution of $|\hat{u}|$ is non-Gaussian with a longer tail for positive numbers. This justifies using a log normal approach for uncertainties, as is common for magnitude scales. For a single peak amplitude measurement at a station of index n at distance r_n, for example, $|\hat{u}^{(n)}|$, the logarithm of the peak amplitude normalised by $|\hat{u}_{\mathrm{syn}}|(r_n)$, can be taken to give a station magnitude. However, for a meaningful source magnitude estimate, a larger number of stations should be considered to average out, for instance, the effects of radiation patterns and rupture directivity.

If N recordings of the event are available (distances r_n, n ranges from 1 to N), the moment magnitude can be defined by

$$\begin{aligned} M_w - M_w^{(\mathrm{r})} &= \log_{10}\left(\frac{M_0}{M_0^{\mathrm{ref}}}\frac{M_0^{\mathrm{ref}}}{M_0^{(\mathrm{r})}}\right)^{2/3} \\ &= \frac{1}{N}\sum_{n=1}^{N}\log_{10}\frac{|\hat{u}^{(n)}|}{|\hat{u}_{\mathrm{syn}}|(r_n)} \\ &- \frac{1}{N}\sum_{n=1}^{N}\log_{10}\frac{\left(\Delta\sigma^{(n)}\right)^{1/3} v_r^{(n)} \cdot w^{(n)} \cdot |\hat{g}^{(n)}|}{\left\langle(\Delta\sigma)^{1/3} v_r \cdot w \cdot |\hat{g}|\right\rangle} . \end{aligned} \tag{8}$$

$M_0^{(r)}$ is a user-selected reference moment for which synthetic seismograms and synthetic attenuation functions are calculated. Kanamori's reference moment M_0^{ref} (Kanamori, 1977) is required to define a moment magnitude M_w (see eq. (1)). The reference moment magnitude $M_w^{(r)}$ is the moment magnitude associated with the user-selected reference moment.

Note that the normalisation factor in the denominator of the second term is averaged over K realised synthetic source models, while the average in the numerator is formed over observations at N stations. If N is large and the azimuthal coverage is good so that directivity effects average out, the second term on the right side can be assumed to be constant C and small or zero, especially if the peak amplitudes are obtained from filtered seismograms. The moment magnitude is then

$$M_w \approx \frac{1}{N}\sum_{n=1}^{N}\log_{10}\frac{|\hat{u}^{(n)}|}{|\hat{u}_{\mathrm{syn}}|(r_n)} + M_w^{(\mathrm{r})} + C . \tag{9}$$

If $M_w^{(\mathrm{r})}$ has been selected close to the magnitude of the studied event, the variance of each station magnitude, $(\delta M_w^{(n)})^2$, can be calculated according to eq. (8). We thereby assume that the measurement of $|\hat{u}|$ is exact (non-varying), but uncertainties in $M_w^{(n)}$ are covered by the bootstrapping of the source and structure models to calculate $|\hat{u}_{\mathrm{syn}}^{(n)}|$. Due to the logarithmic nature of eq. (9), the variance of the station magnitude is $(\delta M_w^{(n)})^2 = \mathrm{Var_n}$. The variance of the mean of the moment magnitude, averaged over all stations, can then be calculated from the variance of the sum of the samples (e.g. Bendat and Piersol, 2010, p. 93-94), meaning the variance of each station magnitude, as

$$\begin{aligned} (\delta M_w)^2 &= \frac{1}{N^2}\sum_{n=1}^{N}(\delta M_w^{(n)})^2 = \frac{1}{N^2}\sum_{n=1}^{N}\mathrm{Var_n} \\ &= \frac{1}{N}\left\{\frac{1}{N}\sum_{n=1}^{N}\mathrm{Var_n}\right\} . \end{aligned} \tag{10}$$

In practice, operational procedures often recommend to use median (MED) and the median of the absolute deviation (MAD) to derive magnitudes and its errors from the sample of station magnitudes (e.g. Di Giacomo and Storchak, 2022; Havskov et al., 2020). In our case, the median estimates for M_w can be considered if the distributions of $M_w^{(n)}$ are collected and MED and MAD are extracted numerically in a single calculation. Another approach is to replace eq. (9) by the formula of a weighted mean, in which weights are defined by the reciprocal variance at each station. Whatever statistical method is used to estimate M_w, our PGD approach to estimate errors differs from the standard procedures because uncertainties of $M_w^{(n)}$ can be estimated at each individual station. From this, the variance of the mean can be calculated, which scales with the reciprocal number of available stations.

We demonstrate the effect in a simulation resembling the geometry of a local network recording mining-induced earthquakes at a depth of only 1 km (Subsection 4.1 below). A hypothetical event with a magnitude of M 1.25 is chosen, randomising the station magnitudes at 18 local stations between 0.05 and 5 km distance. The synthetic attenuation curve $|\hat{u}_{\mathrm{syn}}|(r)$ and its uncertainty were simulated using synthetic seismograms and randomised source models. We then incrementally increase the number of observations (stations) in the simulation test and calculate the mean magnitude and its uncertainty (Fig. 2). While the mean station magnitudes are uniquely defined, the uncertainties differ. The conventional approach estimates the variance of a station magnitude from the ensemble of a larger number of station magnitudes. When only a single station magnitude is available, the variance is indeterminate. In our approach, we calculate the variance of the station magnitude from the bootstrapped source parameters to calculate synthetic seismograms. This allows uncertainties to be reported for a single station observation and, if more than one station is available, the variance of the mean magnitude can be reported. In Fig. 2 the variance of the ensemble of station magnitudes increases with increasing number of stations and finally saturates to a constant variance for about 12 or more stations. In contrast, our approach finds a large variance of the magnitude when only one or two stations are available, which decreases continuously as more stations are added.

Our approach relates to the local magnitude $\mathrm{M_L}$ as follows: $\mathrm{M_L}$ is defined at every station by

$$M_L(r_n) = \log_{10} \frac{|\hat{u}^{(n)}|}{a_0(r_n)}\,, \tag{11}$$

where $|\hat{u}^{(n)}| = \hat{u}(r_n)$ is the peak amplitude measured on the horizontal components of a Wood Anderson seismograph for an epicentral or hypocentral distance of r=30-600 km, and $a_0(r)$ is the attenuation function of a hypothetical reference event with magnitude $\mathrm{M_L}$=0. a_0 has ideally been derived from a large number of earthquake recordings. If $M_w^{(\mathrm{r})}$=0, M_w and M_L should scale linearly with a slope of 1, if the attenuation curve $|\hat{u}_{\mathrm{syn}}|$ is similar to a_0. However, as seen in Fig. 1, the observed M_L-M_w relations are highly non-linear. Deichmann (2006) confirmed the theoretical equivalence between M_L and M_w and discussed potential reasons for the observed discrepancies, which are mainly due to the simplification of wave propagation effects in the procedure for estimating $\mathrm{M_L}$, additionally to source radiation pattern and kinematic rupture effects.

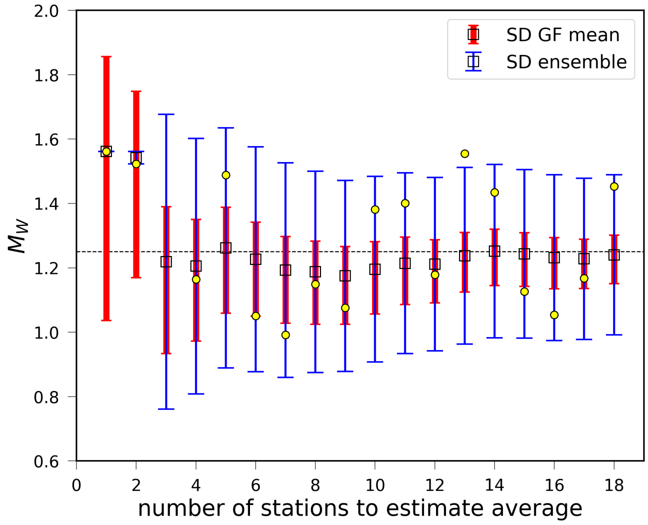

Figure 2 Simulation test to demonstrate the uncertainty estimation. Hypothetical station magnitudes were randomised (normal distribution, σ=0.2) for a local network and a shallow earthquake with M_w=1.25 and z=1 km (yellow circles). The uncertainties of the synthetic attenuation of the peak amplitudes have been calculated according to the described scheme (see Subsection 4.1 for details). Plotted are the mean magnitudes (open squares) and their uncertainties over the number of stations used in the analysis. The standard deviation of the ensemble of station magnitudes (SD ensemble), calculated from station magnitudes only, is represented by the blue error bars. The standard deviation of the mean (SD GF mean, eq. (10)), calculated from bootstrap-derived uncertainties using the Green function (GF) database, is represented by the red error bars. SD ensemble are symmetric around the open squares, and do not provide an error if only one station is available. SD GF mean are asymmetric and provide an error estimate even for a single station. The dashed line indicates M_w=1.25, for which the forward simulation was performed.

An advantage of the synthetic seismogram approach suggested here is that any observed M_L-M_w scaling can be simulated if the synthetic peak amplitudes are extracted in the same way as employed for M_L estimation and if a_0 is given. The forecast of magnitude scaling relations is not restricted to M_L, but can be applied to any magnitude scale M_X, if it is based on peak measurements (see eq. (8)). Fig. S2 (supplementary material) shows simulated M_X-M_w relations in good agreement with relations derived from observations and independent moment determinations (see Fig. 4 in Kanamori, 1983).

3 Implementation

Implementing the theory is computationally intensive and requires efficient numerical tools. The workflow is shown in Fig. 3. In order to generate a queryable database of modelled peak ground motions (PGM) for the determination of moment magnitudes, we simulate waveforms (Heimann et al., 2019) for over 500 random double-couple moment tensors at discrete source depths in a 1D layered velocity model adapted to the region of interest. Records are modelled for each individual source on 20 surface receivers situated at random azimuths and logarithmically distributed distances (Figs 3 and 6).

These synthesised waveforms undergo band-pass filtering within the optimal frequency range for the reference magnitude. Subsequently, ground motion parameters – including peak displacement, velocity, and acceleration amplitudes for both absolute and component-specific (horizontal and vertical) measurements – are extracted. This results in over 10,000 data points representing peak amplitudes derived from random moment tensors for each source depth.

To query modelled peak amplitudes for a specific epicentral distance d and source depth, we consider ensembles that include N nearest peak amplitudes to d. N is configurable and has been set to 25, for example. We determine the average and standard deviation as well as the median value and MAD within these ensembles. This approach extracts relevant information for distance d based on the gridded entries in the database. Further expanding the scope of applicability, we replicate this entire procedure for alternative source depth levels, thereby creating multiple databases covering diverse depth ranges. Linear interpolation between different depth levels permits calculations of peak amplitudes for intermediate source depths with precision. Consequently, the database can be queried for any combination of source depth and distance (Fig. 4) as opposed to the few arbitrary point measurements available from sparse earthquake catalogues.

To account for the potential variability introduced by different reference moment magnitudes ($\mathrm{M_w}^{(r)}$) sampling different frequency ranges, we conduct parallel simulations considering varied reference magnitudes. Post-processing follows suit, applying tailored band-pass frequency filters associated with alternate moment magnitudes.

The procedure is implemented in the Python framework *chimer*, which can generate such ground-motion databases from any Pyrocko GF database (Heimann et al., 2019). For example, the earthquake detection and location framework *qseek* uses this procedure to automatically determine detection magnitudes from peak ground motions (Isken et al., 2024; Büyükakpınar et al., 2024).

4 Applications

4.1 Coal mining in Germany

A first application concerns the Hamm coal mining area in the Ruhr region, NW Germany (Fig. 5). Induced seismicity in the Ruhr region has been monitored over the last 40 years (Bischoff et al., 2009). At Hamm, seismicity induced by longwall mining was continuously monitored by the local HAMNET network (Fig. 5) and more than 7,000 earthquakes were reported over a period of about 1 year, from July 2006 to July 2007 (Bischoff et al., 2009) with local magnitudes spanning between -1.7 and 2.0 (Sen et al., 2013). Most of these earthquakes were shallow and found to occur slightly above the coal seam, which is located at 700 to 1,500 m below the surface (Bischoff et al., 2009). Full waveform moment tensor inversions were performed for more than 1,000 earthquakes, providing moment tensor solutions and moment magnitude estimates (Sen et al., 2013). Here, we consider a subset of 1,133 earthquakes (see catalogue in the supplementary material S4) for which both local magnitudes and moment magnitudes are available.

A first proof of concept is to compare attenuation curves with observed scaled peak ground displacement (PGD). Fig. 6a shows the PGD from all earthquakes, which were scaled to a moment magnitude of 1.25. We calculated mean and standard deviations of the synthetic attenuation curves $|\hat{u}_{\mathrm{syn}}|$ by sampling source depth between z=[1,1.5] km, the rupture velocity between v_r=[1,2] km/s and the stress drop between $\Delta\sigma$ = [1,10] MPa. The average attenuation curve lies well within the scattered observations and its 1σ uncertainty is comparable to the 1σ range estimated from synthetic seismograms. The distance dependence of $|\hat{u}_{\mathrm{syn}}|$ is similar to that of a_0 and absolute values are comparable if a_0 is scaled to a magnitude of $\mathrm{M_L}$=1.5 and if r is interpreted as hypocentral distance.

Fig. 6b shows the effect of source depth on PGD attenuation. As expected, an event occurring at a depth of z=0.5 km features a higher PGD at small epicentral distances than an event with a source depth of z=1.5 km. Thus, the source depth should be considered to obtain unbiased magnitude estimates. While the $\mathrm{M_L}$ scale commonly approximates the source depth by insertion of the hypocentral depth in a_0 (e.g. Bormann et al., 2013), the new methodology presented here considers both the hypocentral depth z and epicentral distance r and is therefore able to account for source- and site-specific depth variation of velocity and intrinsic attenuation Q.

We further verified the concept with two additional tests: first, the theoretically derived $\mathrm{M_L}$-$\mathrm{M_w}$ scaling relation was compared with independent data. Fig. 7a shows a comparison of $\mathrm{M_L}$ magnitudes obtained from standard processing and event location with $\mathrm{M_w}$ derived from full waveform moment tensor inversion (Sen et al., 2013; Cesca and Grigoli, 2015). From the scatter of data points, we calculated parameters of a quadratic regression implementing a maximum likelihood approach, leading to $\mathrm{M_w} = 0.098\mathrm{M_L^2} + 0.48\mathrm{M_L} + 0.44$ valid between -1.5$\leq M_L \leq$2.5. Alternatively, the $\mathrm{M_L}$-$\mathrm{M_w}$ scaling is estimated from the new approach with automatically derived peak amplitudes on Wood Anderson simulated synthetic seismograms, by applying the same attenuation function a_0 (of a hypothetical reference event with magnitude M_L=0) used to calculate $\mathrm{M_L}$. The theoretical scaling agrees well with the empirical scaling, which confirms the stochastic synthetic waveform approach. The additional benefit of the stochastic waveform approach is that realistic uncertainties are derived

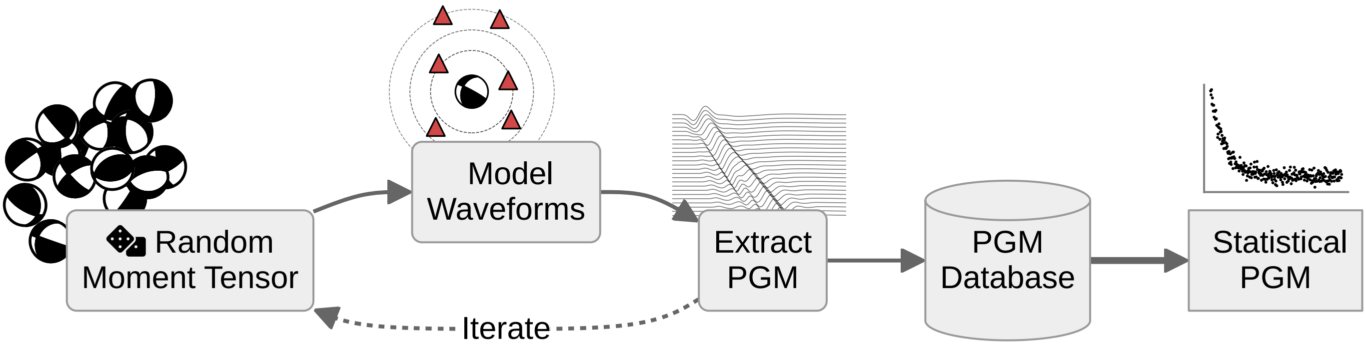

Figure 3 Conceptual generation of peak ground motion (PGM) databases. Synthetic waveforms are modelled for random double-couple moment tensors and random station distributions. Subsequently, PGMs are extracted from simulated waveforms and stored in a database. This database can be queried for statistical distributions of PGMs, e.g. at a given epicentral distance and source depth, the basis for $|\hat{u}_{\mathrm{syn}}|$.

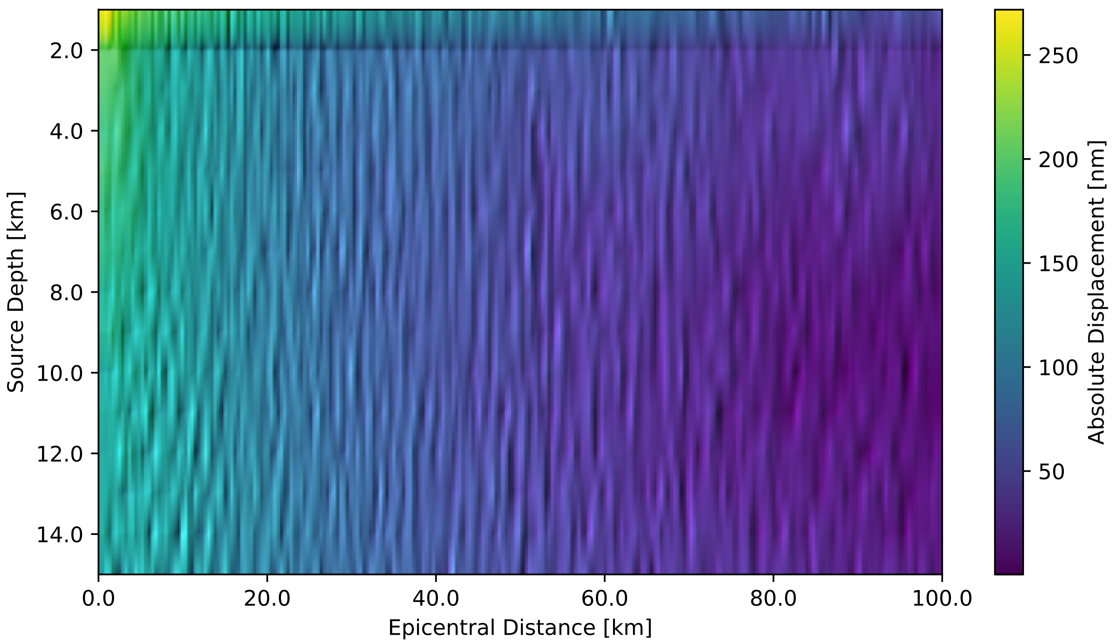

Figure 4 Simulated peak ground motion (PGM) $|\hat{u}_{\mathrm{syn}}|$ (e.g. S- and Rayleigh wave peak in full seismogram) at the surface for different source depths and epicentral distances, visualising the key information stored in the ground motion database. The velocity model shown in Fig. 9 was used. Deeper sources generate smaller ground motions at the surface. The horizontal lineaments are evidence for model layers that interfere with spherical waves emitted from point sources close to the layer boundary. Sources located above the layer boundary produce larger PGMs at the surface because surface waves are efficiently excited.

for the $\mathrm{M_L}$-$\mathrm{M_w}$ scaling, and that the relation is extended to larger or smaller magnitudes for which an extrapolation of empirical data is not possible.

The second test uses automatically determined peak amplitudes from observed seismograms. Before measuring peak amplitudes, different band-pass filters were applied. The stochastic seismogram simulation was used to estimate a representative average attenuation $|\hat{u}_{\mathrm{syn}}|$ for every station and event, which subsequently was employed to derive a station magnitude and its uncertainty. From the ensemble of station magnitudes, the mean $\mathrm{M_w}^{(\mathrm{pgd})}$ and standard deviation $\delta M_w^{(\mathrm{pgd})}$ were derived. In Fig. 7b, $\mathrm{M_w}^{(\mathrm{pgd})}$ is displayed together with $\mathrm{M_w}$ estimates from a full waveform analysis (Sen et al., 2013). An advantage of the peak amplitude $\mathrm{M_w}$ approach is that records from both broadband and short-period stations can be used in an ensemble, since different bandpass filters can be applied to parts of the data.

4.2 Groningen gas field, Netherlands

The second application is to the Groningen gas field in the Netherlands. It represents one of the largest onshore natural gas fields in Europe, producing since the early 1960s (van Thienen-Visser and Breunese, 2015). Of the over 190 exploited gas fields in the Netherlands, only 15% experienced induced seismicity (Van Wees et al., 2014), and only in three fields (Groningen, Bergermeer

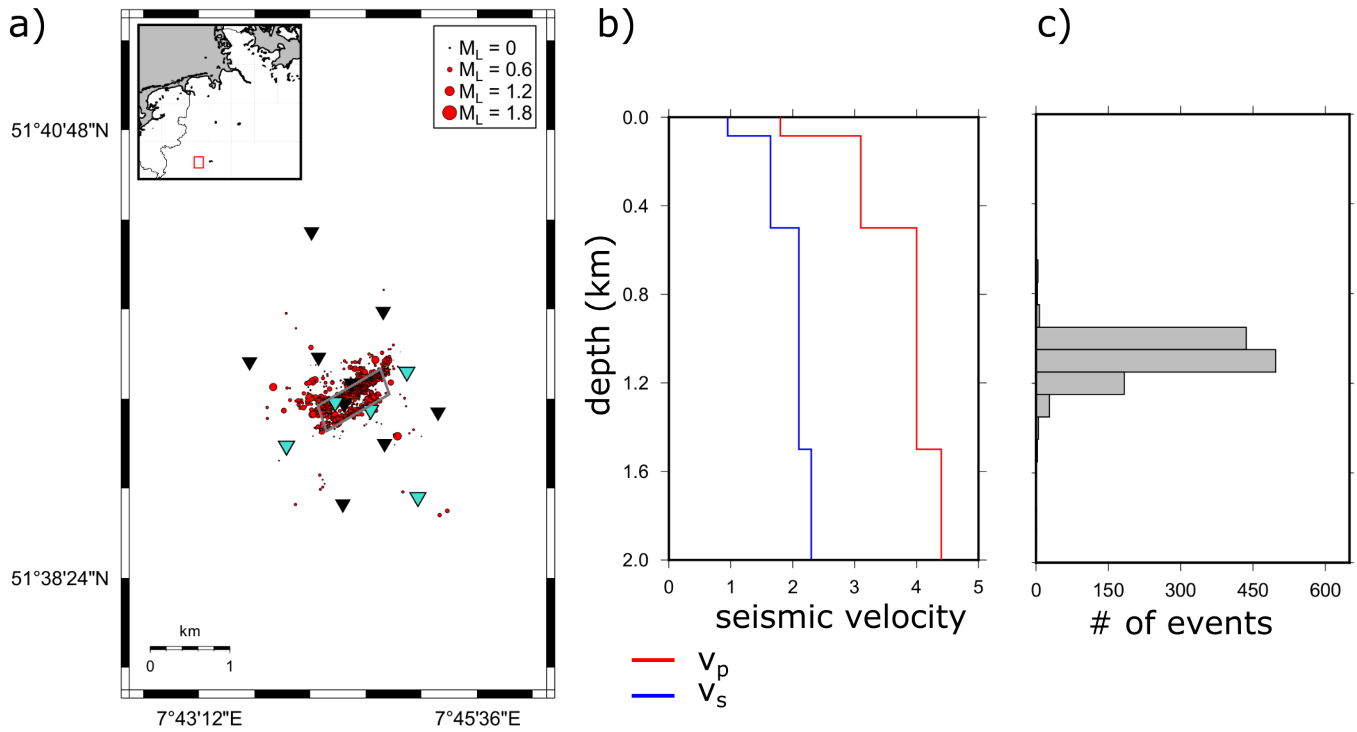

Figure 5 (a) Overview of the Hamm mining play (size of map indicated by red rectangle in inset), epicentres of earthquakes (red circles, size scaled by magnitude), and seismic stations. Light blue and black inverted triangles represent broadband and short-period stations, respectively. (b) Velocity model for P (red line) and S waves (blue line) between 0 and 2 km depth. (c) Depth distribution of located earthquakes.

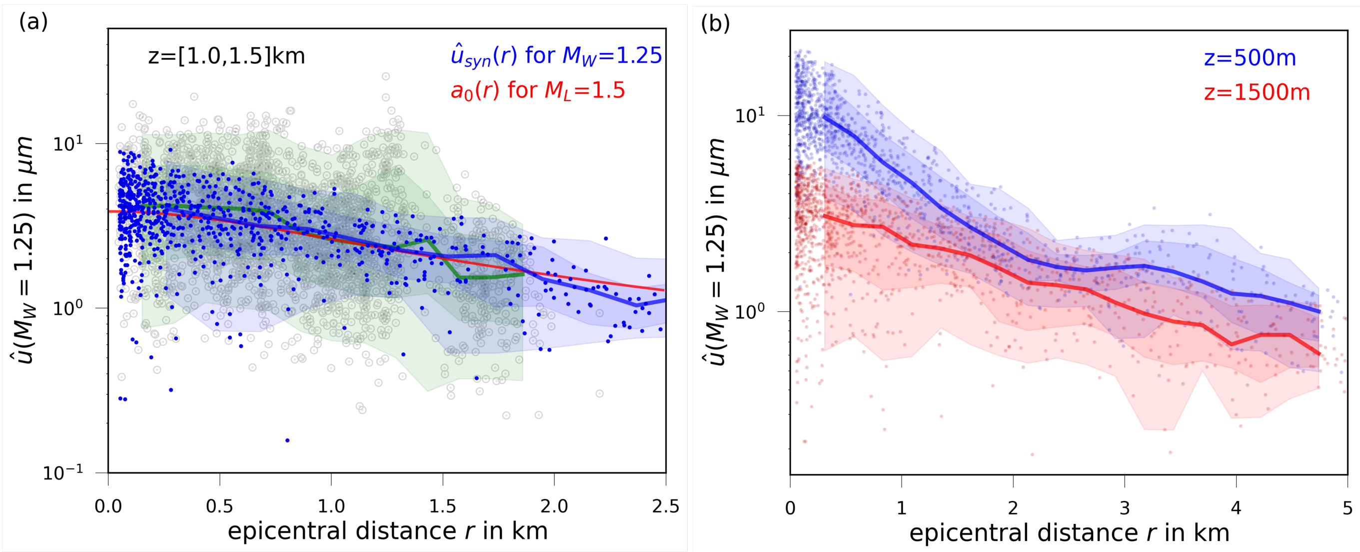

Figure 6 Attenuation curves at local distances for shallow mining-induced seismicity. (a) Comparison of observed peak amplitudes (grey circles) with peak amplitudes derived from synthetic seismograms (blue circles). The source depth was sampled between z=[1,1.5] km, the rupture velocity between v_r=[1,2] km/s, and the stress drop between $\Delta\sigma$ = [1,10] MPa. Mean values indicated by green and blue curves, respectively. 1σ and 2σ indicated by darker and lighter green- and blue-shaded regions. Red curve indicates the attenuation curve given by Richter (1935) to estimate $\mathrm{M_L}$. (b) Extension of synthetic attenuation curves to larger distances. Blue and red circles, curves and shaded regions show peak amplitudes, mean values and 1σ and 2σ of $|\hat{u}_{\mathrm{syn}}|$ for source depths of 500 m and 1500 m, respectively. Distance r is epicentral distance.

and Roswinkel) have events with magnitudes $\mathrm{M_L} \geq 3$ occurred (NAM, 2013). In the vicinity of the Groningen gas field, seismic events started to appear in 1986 and were recognised as induced by the gas production, originating from the declining gas pressure followed by compaction of reservoir rocks resulting in subsidence at the surface and stress changes on the many faults existing in the reservoir (van Thienen-Visser and Breunese, 2015), which is located at a depth of 2,600 – 3,200 m and sealed by Zechstein salt (Bourne et al., 2014). Seismic-

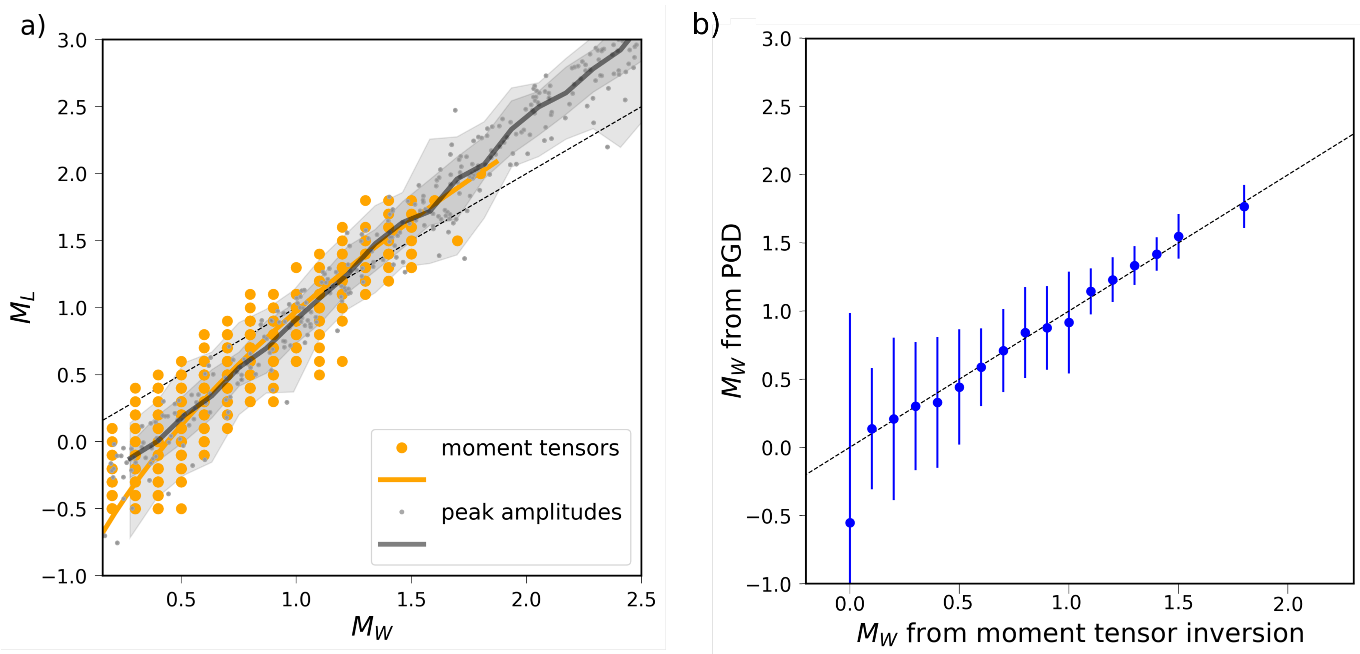

Figure 7 Comparison of magnitudes for the coal mining test-site. (a) The quadratic regression equation (orange curve) estimated from independent measurements of $\mathrm{M_L}$ (see Bischoff et al., 2009) and $\mathrm{M_w}$ (yellow circles, Sen et al., 2013) is compared to the scaling derived from synthetic peak amplitudes (grey circles) and the empirical relation for a_0 (grey curve). 1σ and 2σ based on $\mathrm{M_L}$ estimates are indicated by darker and lighter grey shading. The dashed line indicates $\mathrm{M_L} = \mathrm{M_w}$. (b) Comparison of moment magnitudes derived from full waveform inversion (Sen et al., 2013) and the new peak amplitude approach. Plotted are median (blue dots) and standard deviations (blue vertical bars) derived from binned statistics using 20 equal-sized bins. Peak amplitudes were extracted from both short-period and broadband displacement seismograms recorded on vertical components and filtered between 0.5 and 2 Hz. The dashed line indicates $\mathrm{M_w}$ from PGD=M_w.

ity mainly occurs in regions of high fault density, although it is difficult to relate events to individual faults (Dost et al., 2017). 1,046 events were detected prior to 1 January 2017, 284 of which had magnitudes larger than $\mathrm{M_L}$ 1.5 (Hofman et al., 2017). The strongest event recorded so far ($\mathrm{M_L}$=3.6) occurred on 16 August 2012 in the Huizinge area, causing damage to structures in the province of Groningen (Dost et al., 2017). Fig. 8 displays induced seismicity from 1986 until the 17 January 2018 in the area of the Groningen field (KNMI, 2018).

To illustrate the dependence of magnitude relations on velocity models, we compare predictions for three different 1D velocity models (Fig. 9). The first was extracted from the field operator's (Nederlandse Aardolie Maatschappij, NAM) detailed 3-D elastic model (NAM, 2016) in the region of Loppersum, where most induced events occur (Dost et al., 2017) and was used for a probabilistic moment tensor inversion (Kühn et al., 2020; Dost et al., 2020). The second was employed by Kraaijpoel and Dost (2012) to compute focal mechanisms. The third is an average velocity model used by KNMI for event location in the Northern parts of the Netherlands (Spetzler and Dost, 2017) combined with the CRUST2.0 model (Bassin, 2000) for depths larger than reservoir depth, since the velocity structure of the deeper part of the Carboniferous layer is not well known (Dost et al., 2017). In addition, S wave velocities for the sediments down to 3,000 m depth were estimated from P wave velocities using Castagna's relation (Castagna et al., 1985). Fig. 9c displays hypocentral depths of events after relocation (Spetzler and Dost, 2017) with the equal differential time method (EDT, Lomax, 2005), which reduced the uncertainty in event depth to 300 m. 90% of events take place within the reservoir or top of the underburden, a few weak events with $\mathrm{M_L}$<1 may also occur in the anhydrite layers within the Zechstein seal above the reservoir (Spetzler and Dost, 2017).

In Fig. 10a, we compare the empirical $\mathrm{M_L}$-$\mathrm{M_w}$ scaling relation from Dost et al. (2016) to predictions using our method for these three different 1D velocity models. To this end, we simulated Wood Anderson seismograms for N and E components without any further filter. The uncertainties in source depth, rupture velocity, and stress drop were assumed as z = 2.5 – 4 km, v_r = 1 – 2.25 km/s and $\Delta\sigma$ = 1 – 10 MPa, respectively. From these, the scaling relation derived using the 3rd velocity model fits best the empirical relationship of Dost et al. (2016), which was developed from a collection of earthquakes in the Northern Netherlands.

Local networks to monitor induced seismicity are often deployed directly in the fields or mining areas where earthquakes occur. First P and S waves are clear arrivals at stations above the events, while surface waves have greater amplitudes at larger distances. Traditional $\mathrm{M_L}$ scales do not consider P and S wave peak amplitudes very close to the epicentre. In Fig. 10b, we show theoretical attenuation curves of peak displacements for P and S body waves, measured on vertical and horizontal components, respectively. P waves are expected to have smaller amplitudes than S waves, which is clearly visible. Both P and S wave peak amplitudes attenuate strongly in Groningen within the first 5-10 km from the

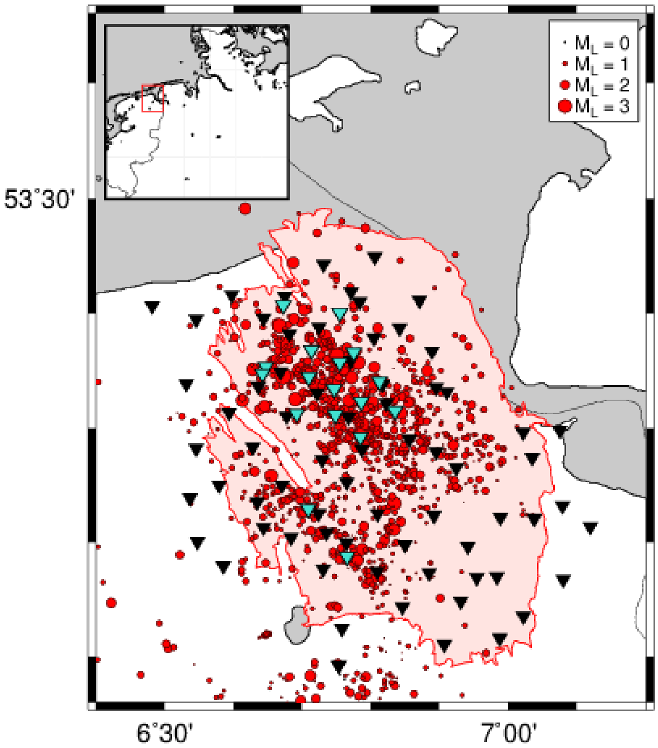

Figure 8 Overview on Groningen gas field induced seismicity. Black triangles indicate shallow borehole stations; turquoise triangles display additional single accelerometer stations. The red polygon shows the extent of the Groningen gas field, and the red circles depict earthquakes induced by gas extraction, where the size scales with magnitude. The size of map is indicated by the red rectangle in the inset.

epicentres due to a strong defocusing effect: only receivers close to the source are reached by direct waves, whereas receivers at larger distances record energy guided within the high-velocity anhydrite layer at the base of the Zechstein evaporites (Kraaijpoel and Dost, 2012; Kühn et al., 2020). However, while the attenuation of S wave peak amplitudes for larger distances r is a smoothly decaying function, the peak amplitudes of P waves increase for distances larger than 35 km. This may be attributed to the total reflections at the impedance contrasts of 6 and 12 km in the Groningen models, together with the effect of an increasing incidence angle leading to smaller amplitudes of longitudinal waves on Z components. The example demonstrates the flexibility of the stochastic simulation approach to consider such body wave phases. The magnitude estimation is not restricted to specific wave types or components. Thus, different wave modes can be integrated in the $\mathrm{M_w}$ estimation.

5 Discussion

Different empirical magnitude scales have evolved over the last hundred years and are commonly used for routine analysis of earthquake strength or seismic hazard and risk assessment. This is particularly the case for moderate and small earthquakes recorded at local distances, for which the local magnitude scale $\mathrm{M_L}$ is still the first reported strength parameter and the number of proposed scales continues to grow, while for large magnitude earthquakes, the physical moment magnitude M_w is now estimated and reported in parallel with the empirical magnitudes. However, even for global earthquakes, research continues on traditional empirical scales such as $\mathrm{M_S}$ or $\mathrm{M_B}$ to maintain consistency with historical earthquake catalogues.

Most empirical magnitude scales are based on measurements of peak amplitudes of ground displacements or ground velocities. Moment magnitudes, or the seismic moments, are estimated from spectral plateaus of wave energy or by fitting low-frequency waveforms. Using peak amplitudes to estimate M_w is not common practice and is not as stable and reliable, leading to larger uncertainties in practice. However, for small earthquakes, peak amplitude measurement is often the only option for automatic processing.

In our study, we investigate if and how peak amplitudes can be used to estimate M_w. Since peak amplitudes are used in the empirical scales, this approach has the advantage of being directly comparable to these traditional scales, and the procedure can be easily implemented into routine processing of seismological surveys without changing established procedures. The new approach mainly replaces the empirical distance-attenuation curves with those derived from synthetic seismograms. Since these synthetic attenuation curves for PGD or PGV are based on a given reference M_w, we propose to estimate M_w from peak amplitudes in a similar way to traditional magnitude scales. The validity of this approach has been theoretically demonstrated for the kinematic model of a circular growing shear crack.

The synthetic attenuation curves are extracted from GF databases and depend on the velocity model and a number of sampled source parameters, such as depth, stress drop, source mechanism, and rupture velocity. Therefore, the attenuation curves can be adapted to a specific site and problem, or used to explore a region that has not previously been affected by earthquakes. The use of synthetic attenuation curves is also flexible to enable selecting only specific channels or time windows of particular phases. Data should be tapered and filtered to preserve high signal-to-noise ratio, selecting low frequency data where possible because they are less sensitive to the selected velocity model, and avoiding very high frequencies well above the earthquake corner frequency, where directivity effects become dominant. The synthetic GFs for generating synthetic attenuation must be treated in the same way as the extraction of peak amplitudes from observed data. If high frequencies above the corner frequency must be considered, the procedure should be calibrated against independently estimated moment magnitudes by adjusting a reference magnitude $M_w^{(r)}$.

However, in order to relate M_w from peak amplitudes to empirical scales such as M_L, the frequency range and the procedure for determining the maximum amplitudes must be carried out according to the respective magnitude scale. The PGM database must be calculated accordingly and cover the required frequency and distance range. Additionally, the reference mag-

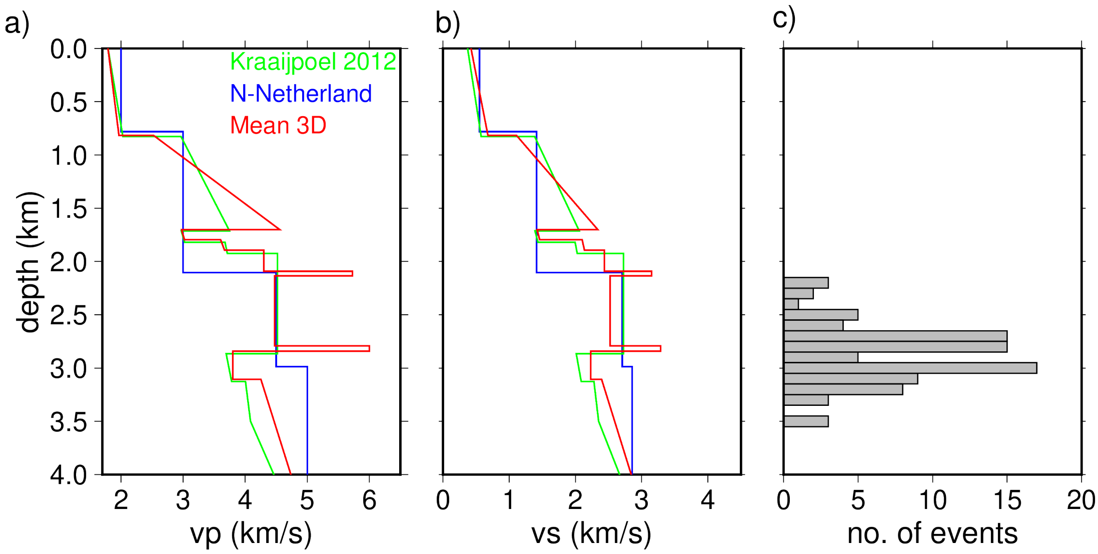

Figure 9 Comparison of velocity models for Groningen. a) P wave velocity profiles; red line: mean 1D velocity model extracted from NAM 3D velocity model in Loppersum area, green line: velocity model employed by Kraaijpoel and Dost (2012) for computation of focal mechanisms, blue line: Northern Netherlands velocity model used by KNMI to locate earthquakes within Groningen field (Spetzler and Dost, 2017). b) S wave velocity profiles. c) Depth distribution of relocated earthquakes listed in Spetzler and Dost (2017).

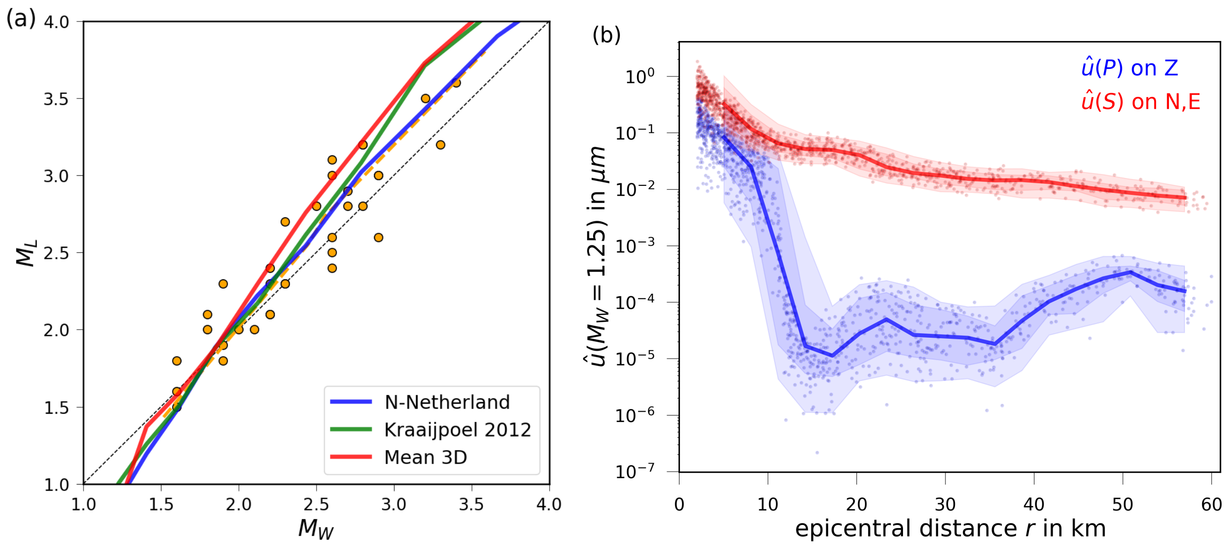

Figure 10 Comparison of magnitudes. (a) The black dashed line indicates $\mathrm{M_L} = \mathrm{M_w}$, while orange circles and dashed line represent observations and the empirical $\mathrm{M_L}$-$\mathrm{M_w}$ relationship by Dost et al. (2016). The solid lines correspond to scaling relations derived from synthetic peak amplitudes applying the empirical relation for a_0 for the three velocity models given in Fig. 9. (b) Synthetic attenuation functions for Groningen region for P (blue) and S waves (red). Blue and red circles, curves and shaded regions show peak amplitudes, mean values and 1σ and 2σ of $|\hat{u}_{\mathrm{syn}}|$, respectively.

nitude $M_w^{(r)}$ must be calibrated to produce a relation comparable with previous estimates. Once the calibration has been performed, even if only employing a few events, conversion scales can be calculated from a purely synthetic experiment and even extrapolated to regions without an earthquake catalogue. This offers the possibility to generate a bundle of $\mathrm{M_x}$ estimates in a parallel routine. For instance, Fig. S2 in the supplementary material shows the predicted conversion of $\mathrm{M_w}$ to teleseismic magnitude scales as $\mathrm{M_S}$ and m_B.

Uncertainties and error handling are important. Conventional empirical magnitude scales often do not document transparent and common procedures for estimating errors, apart from the information that the median or weighted mean or trimmed mean is estimated from station magnitudes. When records from only a few stations are available, or the azimuthal distribution of stations is inadequate, errors in magnitude can be larger than one unit (e.g. Roy et al., 2021). Additionally, if P and S wave amplitudes are used to estimate $\mathrm{M_L}$ at local distances, generic double-couple radiation coefficients may lead to systematic bias and magnitude errors (e.g. Daniel, 2014). Our new approach offers an advantage, because uncertainties in the knowledge of source parameters, structural models, and wave velocities are taken into account when calculating the attenuation curves. Therefore, errors can be assigned even to a magnitude estimated from a single station (station magnitude) in contrast to traditional approaches in which station magnitudes have no formal (independent) errors. However, the more realistic estimation of errors in station networks with large azimuthal gaps cannot hide the fact that the estimated magnitudes then have large uncertainties. The best way to avoid this is to improve the azimuthal coverage of the networks.

The method proposed here is developed for peak amplitudes, but the feature extraction module can be used for various types of waveform attributes, such as for instance envelopes or low-frequency spectra. The GF scheme is numerically more demanding than traditional approaches, since thousands of synthetic seismograms are simulated. An efficient implementation is therefore important. We demonstrate how to take advantage of precomputed GF databases, such as those provided by the Green's Mill project (Heimann et al., 2017, 2019). We provide tools and open software solutions to apply the PGM M_w approach. These software tools offer a simple API to generate simulated PGM at https://chimer.pyrocko.org/, or can be run locally to calculate custom attenuation curves. An online API service will be accessible together with the publication of this article. This extends the online Pyrocko GF services and is in conjunction with the Green's Mill (https://greens-mill.pyrocko.org/) project. Delivering these software tools and online APIs paves the way to implement our proposed method into existing workflows. Alternatively, the method can be implemented by defining an attenuation curve for a given velocity model as a lookup table.

Another aspect concerns the choice of the reference magnitude for which synthetic attenuation curves are calculated. For the determination of the relative strength of an event, the reference magnitude could be arbitrary, as long as the frequency range for the extraction of the peak amplitudes is below the cut-off frequency of the earthquake, which can be ensured by the specifications for the determination of the peak amplitudes. This is the approach taken by existing empirical magnitude scales. However, this would lead to the very limitations we are trying to overcome with the new approach. In addition, the errors of a station's magnitude may be misestimated if the reference magnitude is very far from the true magnitude of the event. An optimal approach would be to choose the reference magnitude for determining the synthetic attenuation curves very close to the true magnitude of the event. However, this leads to increased computational effort or the storage of many PGM databases. In practice, in our experience to date, a compromise is possible by selecting a reference magnitude through tests and comparisons that reproduces the results from independent moment tensor inversions well.

The best possible extraction of peak amplitudes is a general problem that does not only affect the approach here. The choice of window lengths, tapers and bandpass filters can all affect the peak amplitude and estimation of source parameters (e.g. Bindi et al., 2023a,b). We have included an example of how peak amplitudes were extracted using pyrocko in the supplementary material under S3 (see also S2). In general, we recommend that users perform comparative tests depending on the data set and objective, and visually check the results. In any case, it is important to treat the synthetic data in exactly the same way as the observed data.

6 Conclusion

A procedure is proposed to estimate the moment magnitudes of local earthquakes from peak ground displacements using synthetic seismograms from Green's function databases. The validity and applicability of the new method is demonstrated both theoretically and with examples. The new method mitigates some of the shortcomings of traditional magnitude scales, such as saturation, compatibility, or weaknesses in error propagation. The main advantages of the proposed method are:

- its flexibility in employing individual frequency ranges and sensor types, including borehole geophones or, if appropriate Green's function databases are provided, strain rate measurements from DAS,
- its flexibility to consider different wave types, wave modes, and source radiation patterns in parallel,
- its compatibility with traditional scales, allowing conversion relationships to be developed and maintained, even for teleseismic magnitude scales such as $\mathrm{M_S}$ and $\mathrm{m_B}$,
- the realistic estimation of uncertainties even in case of few measurements,
- its flexibility to extrapolate to regions and sites not yet sampled by earthquakes, including the ability to consider 1.5 D velocity models,
- its potential to be extended to higher-frequency signals from even smaller earthquakes.

Acknowledgements

Dr. Samira Mahgsoudi prepared the quadratic regression for Fig. 7 and contributed to discussion in an early version of the paper in 2017. We extensively used Pyrocko - An open-source seismology toolbox and library (Heimann et al., 2017). We are thankful to A. Steinberg and an anonymous reviewers whose comments and questions helped us greatly to improve the manuscript.

Data and code availability

The software for calculating PGM databases `chimer` is available as open source at GitHub https://github.com/pyrocko/chimer (Isken and Heimann, 2024). Critical code review and participation is highly encouraged and welcomed. Software and codes are implemented using the Pyrocko - An open-source seismology toolbox and library (Heimann et al., 2017). Data for the Hamm and

Groningen field are openly available trough FDSN Web-Services (https://www.fdsn.org/networks/detail/Z2_2006, KNMI, 1993).

Competing interests

The authors have no competing interests.

References

Aki, K. Generation and propagation of G waves from the Niigata earthquake of June 1964. *Bull. Earthq. Res. Inst., Univ. Tokyo*, 44:23–88, 1966.

Aki, K. and Richards, P. *Quantitative Seismology, 2nd edition*. W. H. Freeman and Co., San Francisco, 2002.

Al-Ismail, F., Ellsworth, W. L., and Beroza, G. C. Empirical and Synthetic Approaches to the Calibration of the Local Magnitude Scale, ML, in Southern Kansas. *Bulletin of the Seismological Society of America*, 110(2):689 – 697, Mar. 2020. doi: 10.1785/0120190189.

Al-Ismail, F., Ellsworth, W. L., and Beroza, G. C. A Time-Domain Approach for Accurate Spectral Source Estimation with Application to Ridgecrest, California, Earthquakes. *Bulletin of the Seismological Society of America*, 113(3):1091 – 1101, Mar. 2023. doi: 10.1785/0120220228.

Bassin, C. The current limits of resolution for surface wave tomography in North America. *EOS Trans. AGU. 81: Fall Meet. Suppl., Abstract*, 2000.

Bendat, J. S. and Piersol, A. G. *Random Data: Analysis and Measurement Procedures*. Wiley, Jan. 2010. doi: 10.1002/9781118032428.

Bindi, D., Spallarossa, D., Picozzi, M., Oth, A., Morasca, P., and Mayeda, K. The Community Stress-Drop Validation Study—Part I: Source, Propagation, and Site Decomposition of Fourier Spectra. *Seismological Research Letters*, 94((4)):1980 – 1991, 2023a. doi: https://doi.org/10.1785/0220230019.

Bindi, D., Spallarossa, D., Picozzi, M., Oth, A., Morasca, P., and Mayeda, K. The Community Stress-Drop Validation Study—Part II: Uncertainties of the Source Parameters and Stress Drop Analysis. *Seismological Research Letters*, 94((4)):1992 – 2002, 2023b. doi: https://doi.org/10.1785/0220230020.

Bischoff, M., Cete, A., Fritschen, R., and Meier, T. Coal Mining Induced Seismicity in the Ruhr Area, Germany. *Pure and Applied Geophysics*, 167(1 – 2):63 – 75, Dec. 2009. doi: 10.1007/s00024-009-0001-8.

Boore, D. M. The Richter scale: its development and use for determining earthquake source parameters. *Tectonophysics*, 166(1 – 3):1 – 14, Sept. 1989. doi: 10.1016/0040-1951(89)90200-x.

Bormann, P., Wendt, S., and Di Giacomo, D. Seismic sources and source parameters. In Bormann, P., editor, *New Manual of Seismological Observatory Practice (NMSOP-2)*, pages 1–259. GFZ Potsdam, 2013. doi: https://doi.org/10.2312/GFZ.NMSOP-2 $_ch3$.

Bourne, S. J., Oates, S. J., van Elk, J., and Doornhof, D. A seismological model for earthquakes induced by fluid extraction from a subsurface reservoir. *Journal of Geophysical Research: Solid Earth*, 119(12):8991 – 9015, Dec. 2014. doi: 10.1002/2014jb011663.

Browitt, C. EMSC Newsletter No 15. *European-Mediterranean Seismological Centre*, 15:1–12, https://www.emsc–csem.org/Files/docs/data/newsletters/newsletter_15.pdf, 1999.

Brune, J. N. Tectonic stress and the spectra of seismic shear waves from earthquakes. *Journal of Geophysical Research*, 75(26):4997 – 5009, Sept. 1970. doi: 10.1029/jb075i026p04997.

Butcher, A., Luckett, R., Kendall, J.-M., and Baptie, B. Seismic Magnitudes, Corner Frequencies, and Microseismicity: Using Ambient Noise to Correct for High-Frequency Attenuation. *Bulletin of the Seismological Society of America*, 110(3):1260 – 1275, Apr. 2020. doi: 10.1785/0120190032.

Büyükakpınar, P., Isken, M., Heimann, S., Kühn, D., Starke, J., López Comino, J., Cesca, S., Doubravová, J., Gudnason, E., and Ágústsdóttir, T. Understanding the Seismic Signature of Transtensional Opening in the Reykjanes Peninsula Rift Zone, SW Iceland. *Journal of Geophysical Research: Solid Earth*, 2024. doi: 10.1029/2024JB029566.

Castagna, J. P., Batzle, M. L., and Eastwood, R. L. Relationships between compressional-wave and shear-wave velocities in clastic silicate rocks. *Geophysics*, 50(4):571 – 581, Apr. 1985. doi: 10.1190/1.1441933.

Cesca, S. and Grigoli, F. *Full Waveform Seismological Advances for Microseismic Monitoring*, page 169 – 228. Elsevier, 2015. doi: 10.1016/bs.agph.2014.12.002.

Dahm, T. and Krüger, F. Moment tensor inversion and moment tensor interpretation. In Bormann, P., editor, *New Manual of Seismological Observatory Practice (NMSOP-2)*. IASPEI, GFZ German Research Centre for Geosciences, Potsdam, 2012. doi: https://doi.org/10.2312/GFZ.NMSOP-2_IS_3.9.

Daniel, G. Bias in magnitude for earthquakes with unknown focal mechanism. *Geophysical Prospecting*, 62(4):848 – 861, May 2014. doi: 10.1111/1365-2478.12142.

Deichmann, N. Local Magnitude, a Moment Revisited. *Bulletin of the Seismological Society of America*, 96(4A):1267 – 1277, Aug. 2006. doi: 10.1785/0120050115.

Deichmann, N. Theoretical basis for the observed break in ML/MW scaling between small and large earthquakes. *Bulletin of the Seismological Society of America*, 107(2):505 – 520, Feb. 2017. doi: 10.1785/0120160318.

Di Giacomo, D. and Storchak, D. A. One hundred plus years of recomputed surface wave magnitude of shallow global earthquakes. *Earth System Science Data*, 14(2):393 – 409, Feb. 2022. doi: 10.5194/essd-14-393-2022.

Dost, B., Edwards, B., and Bommer, J. Local and Moment magnitudes in the Groningen Field. NAM Report, van Elk, J. and Doornhof, D. (eds.), KNMI and NAM, 2016.

Dost, B., Ruigrok, E., and Spetzler, J. Development of seismicity and probabilistic hazard assessment for the Groningen gas field. *Netherlands Journal of Geosciences*, 96(5):s235 – s245, Dec. 2017. doi: 10.1017/njg.2017.20.

Dost, B., van Stiphout, A., Kühn, D., Kortekaas, M., Ruigrok, E., and Heimann, S. Probabilistic Moment Tensor Inversion for Hydrocarbon-Induced Seismicity in the Groningen Gas Field, the Netherlands, Part 2: Application. *Bulletin of the Seismological Society of America*, 110(5):2112 – 2123, Aug. 2020. doi: 10.1785/0120200076.

Duda, S. and Yanovskaya, T. Spectral amplitude-distance curves for P-waves: effects of velocity and Q-distribution. *Tectonophysics*, 217(3 – 4):255 – 265, Jan. 1993. doi: 10.1016/0040-1951(93)90009-9.

Goertz-Allmann, B., Edwards, B., Bethmann, F., Deichmann, N., Clinton, J., Fäh, D., and Giardini, D. A new empirical magnitude scaling relation for Switzerland. pages 3088–3095, 2011. doi: https://doi.org/10.1785/0120100291.

Grünthal, G., Wahlström, R., and Strohmeyer, D. The Unified Catalogue of Earthquakes in Central, Northern and Northwestern

Europe (Cenec)-updated and expanded to the last millenium. pages 517–541, 2009. doi: https://doi.org/10.1007/s10950-013-9379-y.

Grünthal, G., Wahlström, R., and Strohmeyer, D. The SHARE European earthquake catalogue (SHEEC) for the time period 1900-2006 and its comparison to the European-Mediterranean earthquake catalog (Emec). *Journal of Seismology*, pages 1339–1344, 2013. doi: https://doi.org/10.1007/s10950-013-9379-y.

Hanks, T. C. and Kanamori, H. A moment magnitude scale. *Journal of Geophysical Research: Solid Earth*, 84(B5):2348 – 2350, May 1979. doi: 10.1029/jb084ib05p02348.

Havskov, J., Voss, P. H., and Ottemöller, L. Seismological Observatory Software: 30 Yr of SEISAN. *Seismological Research Letters*, 91(3):1846 – 1852, Mar. 2020. doi: 10.1785/0220190313.

Heimann, S., Kriegerowski, M., Isken, M., Cesca, S., Daout, S., Grigoli, F., Juretzek, C., Megies, T., Nooshiri, N., Steinberg, A., Sudhaus, H., Vasyura-Bathke, H., Willey, T., and Dahm, T. Pyrocko - An open-source seismology toolbox and library, 2017. doi: 10.5880/GFZ.2.1.2017.001.

Heimann, S., Vasyura-Bathke, H., Sudhaus, H., Isken, M. P., Kriegerowski, M., Steinberg, A., and Dahm, T. A Python framework for efficient use of pre-computed Green's functions in seismological and other physical forward and inverse source problems. *Solid Earth*, 10(6):1921 – 1935, Nov. 2019. doi: 10.5194/se-10-1921-2019.

Hofman, L. J., Ruigrok, E., Dost, B., and Paulssen, H. A Shallow Seismic Velocity Model for the Groningen Area in the Netherlands. *Journal of Geophysical Research: Solid Earth*, 122(10): 8035 – 8050, Oct. 2017. doi: 10.1002/2017jb014419.

Isken, M. and Heimann, S. pyrocko/chimer: v0.1.1, 2024. doi: 10.5281/ZENODO.14217554.

Isken, M. P., Dahm, T., Heimann, S., Münchmeyer, J., Cesca, S., and Niemz, P. Advancing Seismic Event Detection: Integrating Machine Learning with Waveform-Stacking Techniques. *EGU General Assembly 2024, Vienna, Austria*, EGU24-18706, 2024. doi: 10.5194/egusphere-egu24-18706.

Jansky, J., Kvasnicka, M., and Duda, S. Discussion of the features of synthetic amplitude-distance curves of teleseismic P-waves for global Earth models. *Studia et Geofisica*, 41:130–148, 1997.

Kanamori, H. The energy release in great earthquakes. *Journal of Geophysical Research*, 82(20):2981 – 2987, July 1977. doi: 10.1029/jb082i020p02981.

Kanamori, H. Magnitude scale and quantification of earthquakes. *Tectonophysics*, 93(3 – 4):185 – 199, Apr. 1983. doi: 10.1016/0040-1951(83)90273-1.

KNMI. Netherlands Seismic and Acoustic Network, 1993. doi: 10.21944/E970FD34-23B9-3411-B366-E4F72877D2C5.

KNMI. Induced seismicity catalogue, 2018. http://www.knmi.nl/kennis-en-datacentrum/dataset/aardbevingscatalogus. accessed 19.01.2018.

Kraaijpoel, D. and Dost, B. Implications of salt-related propagation and mode conversion effects on the analysis of induced seismicity. *Journal of Seismology*, 17(1):95 – 107, June 2012. doi: 10.1007/s10950-012-9309-4.

Kühn, D., Heimann, S., Isken, M. P., Ruigrok, E., and Dost, B. Probabilistic Moment Tensor Inversion for Hydrocarbon-Induced Seismicity in the Groningen Gas Field, The Netherlands, Part 1: Testing. *Bulletin of the Seismological Society of America*, 110(5): 2095 – 2111, Aug. 2020. doi: 10.1785/0120200099.

Lomax, A. A Reanalysis of the Hypocentral Location and Related Observations for the Great 1906 California Earthquake. *Bulletin of the Seismological Society of America*, 95(3):861 – 877, June 2005. doi: 10.1785/0120040141.

Luckett, R., Ottemöller, L., Butcher, A., and Baptie, B. Extending local magnitude $\mathrm{M_L}$ to short distances. *Geophysical Journal International*, 216(2):1145 – 1156, Nov. 2018. doi: 10.1093/gji/ggy484.

NAM. Technical addendum to the winningsplan Groningen 2013: subsidence, induced earthquakes and seismic hazard analysis in the Groningen field. Technical report, Nederlandse Aardolie Maatschappij B.V., 2013.

NAM. Study and data acquisition plan, induced seismicity in Groningen, update postwinningsplan 2016. Technical report EP201604200072, Nederlandse Aardolie Maatschappij B.V., 2016.

Purcaru, G. and Berckhemer, H. A magnitude scale for very large earthquakes. *Tectonophysics*, 49(3 – 4):189 – 198, Sept. 1978. doi: 10.1016/0040-1951(78)90177-4.

Richter, C. F. An instrumental earthquake magnitude scale. *Bulletin of the Seismological Society of America*, 25(1):1 – 32, Jan. 1935. doi: 10.1785/bssa0250010001.

Roy, C., Nowacki, A., Zhang, X., Curtis, A., and Baptie, B. Accounting for Natural Uncertainty Within Monitoring Systems for Induced Seismicity Based on Earthquake Magnitudes. *Frontiers in Earth Science*, 9, May 2021. doi: 10.3389/feart.2021.634688.

Sato, T. and Hirasawa, T. Body wave spectra from propagating shear cracks. *Journal of Physics of the Earth*, 21(4):415 – 431, 1973. doi: 10.4294/jpe1952.21.415.

Sen, A. T., Cesca, S., Bischoff, M., Meier, T., and Dahm, T. Automated full moment tensor inversion of coal mining-induced seismicity. *Geophysical Journal International*, 195(2):1267 – 1281, Aug. 2013. doi: 10.1093/gji/ggt300.

Spetzler, J. and Dost, B. Hypocenter Estimation of Induced Earthquakes in Groningen. *Geophysical Journal International*, page ggx020, Jan. 2017. doi: 10.1093/gji/ggx020.

Stork, A., Verdon, J., and Kendall, J. The robustness of seismic moment and magnitudes estimated using spectral analysis. *Geophysical Prospecting*, 62(4):862 – 878, May 2014. doi: 10.1111/1365-2478.12134.

Udías, A., Madariaga, R., and Buforn, E. *Source Mechanisms of Earthquakes: Theory and Practice*. Cambridge University Press, Apr. 2014. doi: 10.1017/cbo9781139628792.

Utsu, T. *Relationships between magnitude scales*, page 733 – 746. Elsevier, 2002. doi: 10.1016/s0074-6142(02)80247-9.

van Thienen-Visser, K. and Breunese, J. N. Induced seismicity of the Groningen gas field: History and recent developments. *The Leading Edge*, 34(6):664 – 671, June 2015. doi: 10.1190/tle34060664.1.

Van Wees, J., Buijze, L., Van Thienen-Visser, K., Nepveu, M., Wassing, B., Orlic, B., and Fokker, P. Geomechanics response and induced seismicity during gas field depletion in the Netherlands. *Geothermics*, 52:206 – 219, Oct. 2014. doi: 10.1016/j.geothermics.2014.05.004.